The effect of size and shape-dependent optical properties on colored radiative cooling in metal island films

Refet A Yalcin, Cagatay Haratoka, S. Camelio, David Babonneau, Karl Joulain, Jérémie Drevillon

The effect of size and shape-dependent optical properties on colored radiative cooling in metal island films.

Refet A. Yalcin, Cagatay Haratoka, David Babonneau, Sophie Camelio, Karl Joulain, Jeremie Drevillon

Université de Poitiers, ISAE-ENSMA, CNRS, PPRIME, Poitiers, France

Abstract

We study visible and infrared optical absorption of metal island films that are commonly used for applications such as color filters and sensors. Calculations were performed using the T-matrix method and compared to experimental transmittance measurements at visible spectrum on a real sample. While the radiation transfer solution through these films often assumes (i) no plasmon coupling, (ii) spherical particles, (iii) monodispersed size particles and/or (iv) bulk refractive index, we carefully study the influence of these assumptions on spectral transmittance. After a validation of the method, the resulting performance in terms of solar energy absorption, color lightness and hue are evaluated on a radiative cooling structure. Alternative designs that provide stronger coloration and thermal performance are proposed and discussed.

1. Introduction

Radiative cooling is the radiative heat exchange between an object and the space which is at 3K. As demonstrated earlier[1], an object can passively cool below ambient temperature even under direct sunlight. In order to perform efficiently, radiative coolers are expected to be spectrally selective. For radiative cooling applications, objects should be reflective in the solar spectrum and emissive in the infrared, especially at wavelengths between 8 and 13 μm where the atmosphere is transparent. As a result of high solar reflectance, effective radiative coolers have whitish colors. However, due to aesthetic purposes, different works have considered the design of colored

radiative coolers[2,3]. The challenge to introduce color into radiative coolers lies in performing a trade-off between thermal performance and color intensity (lightness)[2]. Color is introduced by absorption of light in the visible spectrum which also increases the absorbed solar heat flux and decreases the thermal efficiency of radiative coolers. Having a narrow absorption peak is therefore an efficient way in order to obtain low solar absorption coloration. Metal nanoparticles (NPs) are good candidates for this application[2]. Nevertheless, effects of localized surface plasmons and plasmon coupling, that can negatively affect thermal and visual performance of the radiative coolers, should be further investigated.

Metal island films consisting of metal particles dispersed on a dielectric surface are known to exhibit absorbance peaks in the visible range due to the excitation of localized surface plasmons when interacting with light. They have a wide application range such as spectrally selective solar light absorbing[4], filtering[5], sensing applications[6] and catalyzing the growth of unidimensional objects such as carbon nanotubes[7].

While simulating the light transfer through metal NPs in a plane, because of the complexity and computational intensiveness of the problem, several assumptions are usually performed such as; (i) neglecting the coupling effects between neighboring particles, (ii) assuming spherical particles, (iii) using monodispersed particles, (iv) using bulk refractive index. The present study aims to identify the accuracy of these assumptions while simulating light transfer in a plane-parallel slab of layered silver NPs that are small (typically below 10 nm in radius). Finally, an alternate approach to achieve colorization introducing thin film filters to radiative coolers is proposed for a better thermal and visual performance.

2. Background

2.1.Solution of Maxwell's equations

Solution of Maxwell's equations for a single sphere under plane wave excitation was developed by Gustav Mie[8] and known as Lorenz-Mie theory. The solution was later extended[9] for cylinders and spheroids. In a medium where the NPs are well-separated from each other the so-called "independent scattering assumption" can be applied [10]. Under this assumption, superposition of the absorption cross-sections of separate particles that are calculated by Lorenz-

Mie theory can be superposed to find the total absorption cross-section of the domain. This approach does not account for the coupling effects among the neighboring particles and particle, surface interaction.

Lorenz-Mie theory applies to a single particle in vacuum. Electromagnetic wave transport in heterogeneous structures, such as NP layers is also governed by Maxwell's equations. Solution of these equations in complex structures can be obtained by various methods including the finite difference time domain (FDTD)[11], the discrete dipole approximation (DDA)[12], the finite element (FEM)[13], and the superposition T-matrix[14] methods. In all these methods the problem gets computationally more expensive when metallic NPs are involved, distance between them gets smaller and the number of particles as well as size of the domain with respect to the incident wavelength gets larger. As a result, a proper method in terms of accuracy, computational resource usage and computational time should be selected. The T-matrix method is known to be an effective method compared to the others[15]. Some software based on the T-matrix method like Smuthi[16] and CELES[17] are also profited from GPU acceleration that bring down computation times up to 100-fold for systems with large number of particles.

2.2.Size dependent refractive index

A common approach while setting the refractive index of NPs is to use bulk refractive index. For NPs under 20 nm radii, the dielectric function of metals becomes size dependent and as the particle size gets smaller, the refractive index of the NP deviates more from the bulk material's optical properties[18]. Size dependency accounts for both intraband transitions (free electrons) and interband transitions (bound electrons). The modification that arises from bound electrons is significant only for NPs smaller than 2 nm as pointed out by Herrera *et al*. [18]. Since NPs smaller than 2 nm cannot be determined accurately with the applied methods in this study, interband transitions were not considered. Only free electron contribution was considered in this study for the size dependent dielectric function which is given by[18]:

$$\varepsilon\left(\omega, r_{eff}\right) = \varepsilon_{bulk}(\omega) - \omega_p^2 \sum_{n=1}^{\infty} (-1)^n \frac{\left(\frac{i\omega A v_F}{r_{eff}}\right)^n}{\left(\omega^2 + i\omega\gamma_{free}\right)^{n+1}} \tag{1}$$

where r_{eff} and ω, ω_p, γ_{free}, A, v_f are effective radius of the particle, electromagnetic wave frequency, plasma frequency, damping constant (for noble metals $A \approx 0.8$), and Fermi velocity respectively.

2.3.Radiative cooling

Main driving power of the radiative cooling is the outgoing hemispherical radiation P''_{rad} from the coating. Nighttime radiative cooling heat flux of the coating can be found by subtracting the atmospheric heat flux gain P''_{atm} from the P''_{rad}. Daylight radiative cooling incorporates solar effects. Solar absorption of the coating, P''_{solar}, should be further subtracted from P''_{rad} to find daytime radiative cooling P''_{cool} of the coating which reads:

$$P''_{cool} = P''_{rad} - P''_{atm} - P''_{solar}. \quad (2)$$

With the help of Kirchhoff's law, $\alpha(\lambda,\theta) = \epsilon(\lambda,\theta)$, components of the net radiative cooling in **Eq. 2** can be calculated from;

$$P''_{rad} = \int_{2\pi}\int_{0}^{\infty} I_{bb}(\lambda,T)_{T=T_{sur}}\, \epsilon(\lambda,\theta)\cos(\theta)\, d\lambda d\Omega \quad (3)$$

$$P''_{atm} = \int_{2\pi}\int_{0}^{\infty} I_{bb}(\lambda,T)_{T=T_{amb}}\, \alpha(\lambda,\theta)\epsilon_{atm}(\lambda,\theta)\cos(\theta)\, d\lambda d\Omega \quad (4)$$

$$P''_{solar} = \int_{0}^{\infty} I_{Solar}(\lambda)\, \alpha(\lambda,\theta)_{\theta=0} d\lambda \quad (5)$$

where,

$$\epsilon_{atm}(\lambda,\theta) = 1 - \tau_{atm}(\lambda)^{1/\cos(\theta)} \quad (6)$$

Here, $\tau_{atm}(\lambda)$ is the atmospheric transmittance, I_{solar} is normal direct irradiance, $I_{bb,Tsur}$ is the blackbody intensity at the surface temperature.

3. Analysis

3.1.Problem statement

Figure 1 illustrates the silver metallic islands exposed to visible light investigated in the present study and the different parameters considered. The structure was characterized by (i) shape of the particles, (ii) size distribution of the particles, (iii) the particle spatial arrangement, (iv) the particle refractive index, and (v) the continuous medium refractive index at wavelength λ.

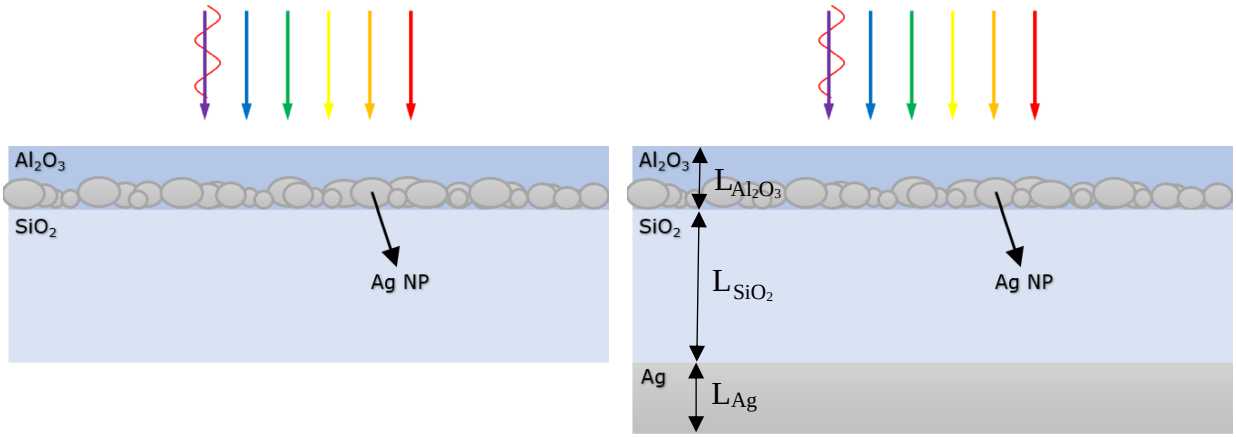

(a) (b)

Figure 1. Illustration of (a) metal island layer composed of silver NPs deposited on silica and capped with Al_2O_3, (b) back face of the silica substrate is coated with silver. $L_{Al_2O_3}$ = 20 nm, L_{SiO_2} = 500 µm, L_{Ag} = 300 nm.

Table 1 lists the investigated cases of the study; (i) assuming oblate spheroid and (ii) spherical particles (iii) using monodispersed particles, and (iv) assuming bulk refractive index. The measured spectral transmittance of the real sample is compared with the calculated transmittance that are accounting for the defined cases. Finally, an additional case study, that weakens the coupling effects between neighboring particles by changing the vertical positions of particles and increasing the minimum distance, c_{min}, between them, was carried out.

Table 1. The investigated cases in this study.

Case name	Particle shape	Particle size distribution	Refractive index
Real sample		Polydisperse	Size dependent
Spheroid assumption	Oblate spheroid	Polydisperse	Size dependent
Sphere assumption	Sphere	Polydisperse	Size dependent
Monodisperse assumption	Oblate spheroid	Monodisperse	Size dependent
Bulk ref. index assumption	Oblate spheroid	Polydisperse	Bulk data

3.2.HAADF-STEM image digitization

The location and size of the particles were digitized by using circular Hough transform[19]. **Figure 2** shows the plane-view HAADF-STEM (high-angle annular dark-field imaging - scanning transmission electron microscopy) image. The silver layer consists of a polydisperse assembly of NPs whose shape can be approximated to oblate spheroids with a long axis a (in-plane) and a short axis c (out-of-plane). For spheroids, effective radius is calculated as $r_{eff} = \sqrt[3]{a \cdot a \cdot c}$. The location

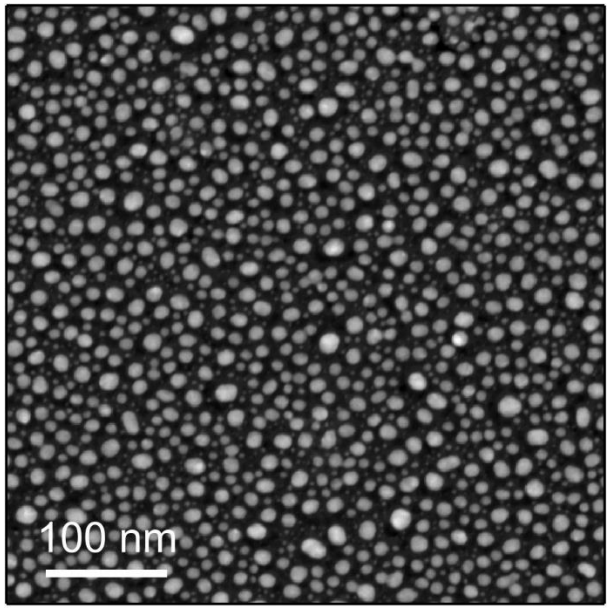

Figure 2. HAADF-STEM image of the sample.

and in-plane size of the particles were identified by digitizing the HAADF-STEM image with surface area L x L using circular Hough transform[19]. Moreover, in addition to the in-plane size distribution, quantitative information about the height of the particles can be obtained from the intensity distribution in the HAADF-STEM image[20]. A correlation exists between a and c as

$$\begin{aligned} c = f_c(\mathrm{a}) = \ 0.36\ a\ +\ 1.27\ \mathrm{nm} \qquad & \text{if } a > 2.5\ \mathrm{nm} \\ c = \ f_c(\mathrm{a}) = a \qquad & \text{otherwise} \end{aligned} \tag{7}$$

3.3.Monodisperse assumption

A single volume averaged particle with periodic boundary conditions is considered to represent all of the metal islands. This approach can be preferred since modelling a high number of spheroids is computationally expensive. The volume equivalent average radius r_{vol}, can be calculated as;

$$r_{vol} = \sqrt[3]{\frac{\sum_{k=1}^{N_p}(a_k \cdot a_k \cdot c_k)}{N_p}} \tag{8}$$

Here, the in-plane area (L_{vol} x L_{vol}) of the periodic domain was found by keeping the silver volume per unit area constant which yielded;

$$\frac{r_{vol} \cdot r_{vol} \cdot f_c(r_{vol})}{L_{vol}\ x\ L_{vol}} = \frac{\sum_{k=1}^{N_p}(a_k \cdot a_k \cdot c_k)}{L\ x\ L} \tag{9}$$

Following **Equations (7)** and **(8)**, the volume equivalent average radius, r_{vol} = 5.92 nm and corresponding short axis $c = f_c(r_{vol})$ = 3.40 nm was found. Side of the periodic square domain was also found from **Equation (9)** as L_{vol} = 7.66 nm for the monodisperse assumption case calculations.

3.4.Methods of solution

In the current study, we implemented open-source Python code Smuthi[16] for utilizing the T-matrix method. The script creates the metal islands by reading the spatial coordinates, [x_k, y_k, z_k]

and radius, a_k. Then short axis of spheroids, c_k, **(Equation 7)** and size dependent refractive indices of particles **(Equation 1)** are calculated. Finally, the script solves Maxwell's equations using the software Smuthi and calculates transmittance and reflectance. A recently developed approach[21] to implement periodic boundary condition capability to the T-matrix method is used to investigate the effect of monodisperse assumption.

The T-matrix method cannot solve particles with intersecting surfaces. **Figure S2** illustrates the geometries which T-matrix can and cannot be used to solve. Intersecting spheroids are removed from the digitized dataset before utilizing the T-matrix method. Particles that are smaller than 2 nm cannot be determined accurately with the applied methods in this study, therefore they are removed too. After the circular Hough transform digitizes the HAADF-STEM image, the particle data list is ordered from largest sized circle to smallest. Then starting from the largest one, each circle is controlled with other circles to see if there is an overlap. In case of an overlap, the smaller one of the overlapped particles is omitted. With this algorithm, larger circles are prioritized while removing the overlapping circle. **Figure 3(c)** illustrates the spatial particle distribution, where the intersected and small ones are omitted, the omitted 8 particles constitute less than 0.5% of the particles in the disk in terms of mass, which is insignificant. The finalized digitized particulate disk (**Figure 3(c)**) is considered while calculating the spectral transmittance using the T-matrix method. Particles are considered sitting on the silica layer as illustrated in **Figure 1**, therefore particle-substrate interaction is accounted for. We further calculate extinction cross sections of different sized particles on silica and alumina. Since the surrounding (capping) medium is also alumina, the simulations considering particles sitting over alumina disregards particle-substrate interaction. Figure S4(c) illustrates the low difference between two approaches and we attribute weak particle-substrate interaction to low refractive index mismatch between silica and alumina at the spectrum of interest.

We performed a preliminary study to determine which maximum spherical harmonics order, l_{max}, to use in our study. Light transfer through the original monolayer design was solved at different l_{max}, from 1 to 5. Their root mean square errors are found for 1 to 4 respectively; 6.8%, 5.5%, 2.2%, 1.2% with respect to $l_{max} = 5$. $l_{max} > 5$ cases could not be investigated due to excess RAM requirement of 824 particles. $l_{max} = 4$ is selected and applied for each case in this study since the error it produced was found to be low enough.

Transmittance and reflectance of the metal island layer in Al_2O_3 that is presented in **Figure 3(c)** are calculated by exposing the metal island with a gaussian beam having a beam waist, ω_0, equal to the particulate disk radius, L/2 = 247 nm. The particles outside of the inscribed circle are not considered in order to reduce computational load. The resulting change in particles' spatial distribution can be observed by comparing **Figure 3(a)** and **Figure 3(b)**. Considering power of a gaussian beam passing through a circle of radius r in the transverse plane at position z is:

$$P(r,z) = P_0[1 - e^{-2r^2/\omega^2(z)}] \tag{10}$$

where

$$P_0 = \frac{1}{2}\pi I_0 \omega_0^2 \tag{11}$$

In that case, $r = \omega$, the power passed through the circle becomes $\frac{P(z)}{P_0} = 1 - e^{-2} = 0.8647$

It means that 13.53% of the gaussian beam's intensity pass through from outside of the circle that contains metal islands **(Figure 3(c))**. Therefore, a correction is applied to the spectral transmittance, $T_{matrix,\lambda,}$ and reflectance $R_{matrix,\lambda,}$ that are calculated by the T-matrix method. Corrected spectral transmittance of particulate layer, T_λ, and reflectance, R_λ, are calculated as;

$$T_\lambda = \frac{T_{matrix,\lambda}}{1 - e^{-2}} + \left(1 - \frac{1}{1 - e^{-2}}\right) \tag{12}$$

$$R_\lambda = \frac{R_{matrix,\lambda}}{1 - e^{-2}} \tag{13}$$

For thickness with orders of magnitude larger than the incident wavelength, there are instabilities at the T-matrix method due to interference. As a result, the ray tracing approach detailed in [22] was adopted to account for the boundary reflection effects. In this approach, we consider 1D ray tracing since (i) scattering is small, at least with one order of magnitude, compared to absorption as presented in Figure S4(d) and (ii) the appearance of the sample is not translucent but clear. Sample reflects the light specularly as presented in Figure S3. At the solar spectrum, we consider a 5-layer model; air, alumina, pigmented layer, silica, and silver. Boundary reflections between air-alumina and silica – silver found by Fresnel formalism. Spectral absorption in these non-scattering layers is calculated by Beer-Lambert law, $A_\lambda = 1 - \exp(-4 \cdot \pi \cdot k_\lambda \cdot L/\lambda)$. Here k_λ is the spectral imaginary refractive index of the layer. On the other hand, absorption in the non-

homogenous pigmented layer and reflection on its boundaries are calculated from the T-matrix calculations and then implemented to the ray tracing calculations. Between 2.5 μm – 20 μm spectra, by running the T-matrix simulations we found pigmented layer neither absorbs nor reflects the light; therefore, we disregard particles and consider 4-layer structure for emissivity calculations; air, alumina, silica, and silver. Bulk components of the refractive index of silver and silica were obtained from Wu *et al.*[23] and Kitamura *et al.*[24] Refractive index of alumina was retrieved from ellipsometric measurements on an Al_2O_3 thin film grown on a silicon substrate.

4. Material and Methods

4.1.Sample Preparation, Materials, and Characterization

In the present study, silver island film deposited onto amorphous substrates (carbon-coated copper grids for transmission electron microscopy and fused silica for optical measurements as sketched in **Figure 1(a)**) were fabricated. Silver NPs capped with Al_2O_3 layers were prepared at 200 °C in an ultrahigh vacuum chamber (2×10^{-8} mbar before deposition) by electron-beam evaporation[20]. In the first step, a thin metal layer was grown (nominal thickness t = 3 nm, deposition rate 0.03 nm/s) with the aim of forming the metal island by a Volmer Weber growth mechanism. Then, after a delay time of 30 min, the nano islands were covered with a 20-nm-thick Al_2O_3 capping layer (deposition rate 0.05 nm/s).

The morphology (size and shape) and organization (interparticle distance) of the resulting capped NPs were investigated from in-plane views by high-angle annular dark field scanning transmission electron microscopy (HAADF-STEM) performed with a JEOL 2200FS microscope operated at 200 kV (probe size of 1.5 nm and inner collection angle of 50 mrad). Structural information retrieved from the analysis of the plane-view HAADF-STEM images were used as input parameters to simulate optical transmittance spectra and radiative cooling properties.

4.2.Transmittance Measurements.

The far-field optical response of the capped NPs grown on fused silica substrates (**Figure 1(a)**) was investigated by transmittance measurements at normal incidence (specular beam with

diameter ~3 mm, forward direction) in the spectral range between 350 nm and 800 nm with a 5 nm monochromator step. Integrating sphere is not used since the material is not translucent but transparent. After coating it with silver, we observed that it also reflects the light specularly as we presented in **Figure S3**.

5. Results and Discussion

5.1.HAADF-STEM image digitization and post process

Providing the accurate spatial coordinates and particle size is crucial while simulating the spectral transmittance of the layer composed of silver NPs. From the initial digitization to the final state as the data is provided to the T-matrix method, the following steps are taken. First, the HAADF-STEM image is digitized (**Figure 3(a)**). Then, the particles that lie outside of the inner tangent circle are removed (**Figure 3(b)**) as the particle layer is exposed to a gaussian beam which is circular by definition. Finally, particles that are smaller than 2 nm and smaller of the intersecting particles are omitted (**Figure 3(c)**). The reason for omitting those particles is described in subsection "methods of solution" and is not repeated here for brevity. The resulting particles, N_p = 824 spheroids, are illustrated in **Figure 3(c)** and their size distribution is illustrated in **Figure 4**.

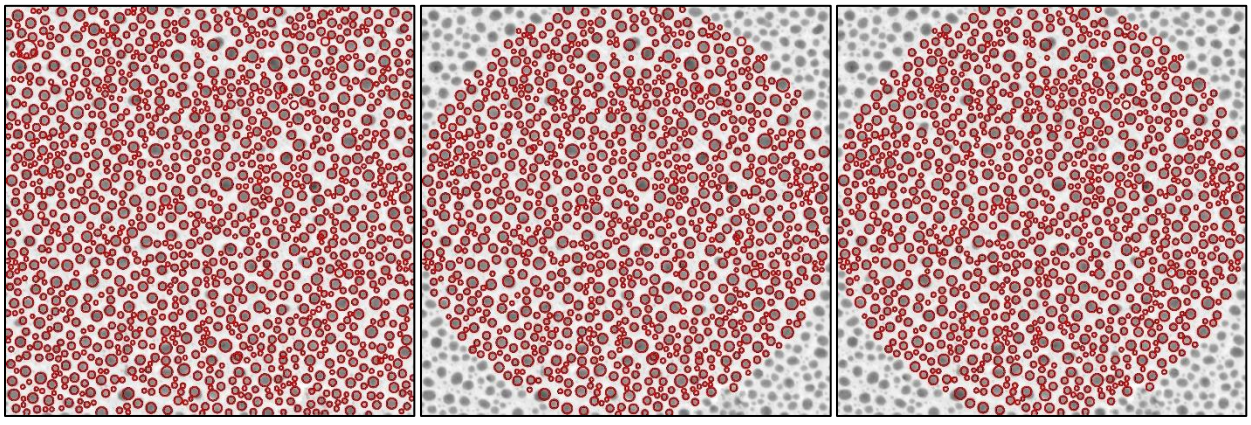

(a) (b) (c)

Figure 3. (a) Digitized HAADF-STEM image, (b) the NPs inside the inner tangent circle of the HAADF-STEM image. (c) NPs that are accounted for in the T-matrix method. Smaller of the intersecting particles are omitted.

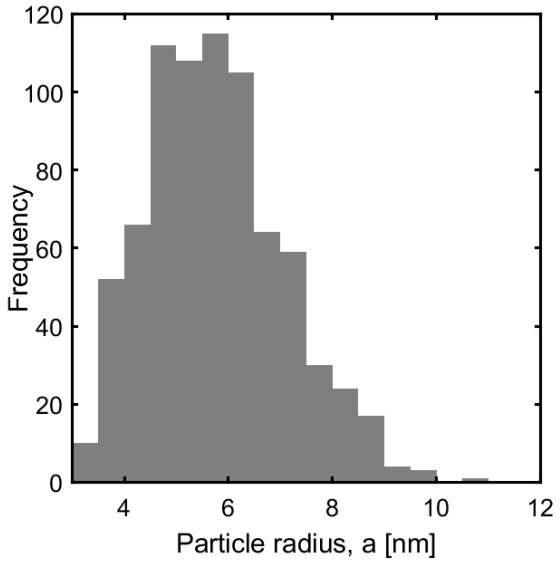

Figure 4. Particle size distribution of silver NPs.

5.2.Radiative cooling calculations

The calculated spectral emittance of the radiative cooler (**Figure 1(b)**) between 2 – 25 μm is presented in **Figure 5**. Corresponding daytime radiative cooling without solar absorption is $P''_{rad} - P''_{atm}$ = 137.5 W m^{-2}. Solar heat flux absorption, P''_{solar}, due to the 500 μm silica layer and silver reflector is around 47 W m^{-2}. Therefore, the baseline, the power flux of the whitish radiative cooler in this study, has a P''_{cool} = 90.6 W m^{-2}.

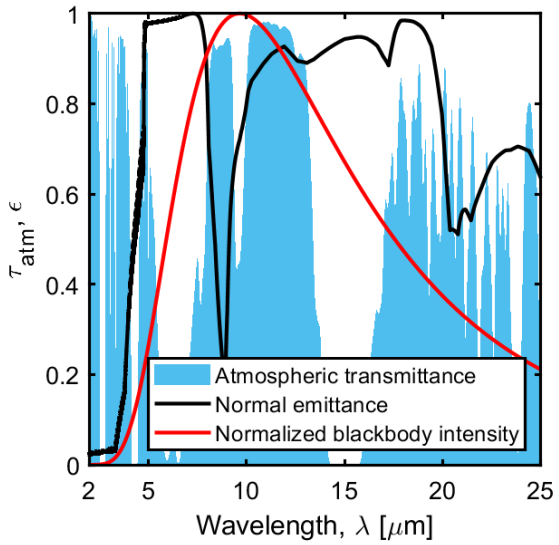

Figure 5. Spectral atmospheric transmittance, emittance and blackbody intensity at T = 300 K.

5.3.Effect of shape, size distribution and using size dependent refractive index

Here, we investigated the effects of aforementioned assumptions listed in **Table 1**. For this, we compared the calculated transmittances of different cases with experimental measurements of the real sample, which exhibits a dip in transmittance located around λ = 515 nm (**Figure 6**). The optical model of the approximated cases was constructed based on the real sample design that is presented in **Figure 1(a)**. First, we investigated the effect of using spherical particles instead of spheroids on spectral transmittance. **Figure 6** shows that a deeper dip in transmittance occurs for the "sphere assumption" compared to the "real sample", which can be attributed to an overestimation of the total amount of silver when spheres are considered. Furthermore, we can see that using spheres instead of oblate spheroids causes a significant blueshift of the surface plasmon resonance, as expected [9].

Using the bulk refractive index instead of the size dependent one is the common practice since defining each sphere in the design with a different refractive index is a tedious process. The result of the "bulk refractive index assumption" case study is also presented in **Figure 6 and Table 2**, which show that use of size dependent refractive index is required for better accuracy, especially at the spectrum where transmittance dip was observed. The wiggles around the dip disappeared and absorption at the peak damped after the utilization of size dependent refractive index as expected [25]. **Figure S4(a)** illustrates size dependent and bulk refractive indices whereas **Figure S4(b)** illustrates extinction cross sections of single particles at different radii that consider size dependent and bulk refractive indices. Results show that peaks are narrower with bulk refractive index compared to size dependent ones, which results in wiggles at transmittance calculations. We attribute these wiggles to the limited number of spheres considered in simulations. Especially absorption is expected to be dominated by the particles at the center of the disk where gaussian beam's intensity is stronger. It is worth to note that, for the spectrum between 430 and 460 nm, the T-matrix method did not converge for the bulk refractive index assumption case and the data among this portion was linearly interpolated.

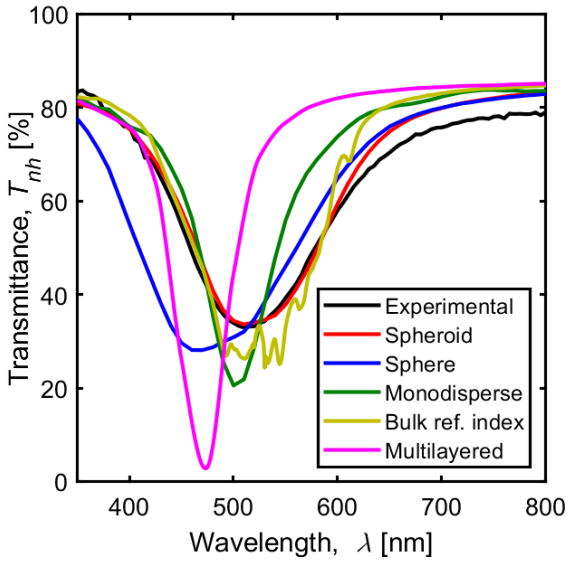

Figure 6. Experimental and calculated transmittance spectra at normal incidence. Numerical results were obtained by considering the cases listed in **Table 1**.

We observed a considerable difference of spectral transmittance between the monodisperse case and the real case. Monodisperse distribution assumption predicted a narrower and a deeper dip at transmittance. Here, we should note that the monodisperse case was not only considering a single sized spheroid that disregards particle size distribution, but also assumes that the location of each particle is well aligned like a photonic structure.

Spheroid particle assumption resulted in a relatively accurate result with a root mean square error less than 3%. The location and width of the transmittance dip compared to the real case is also promising. The outcomes show that spheroid assumption is acceptable and enables the experimental data to be fairly well-reproduced by the T-matrix method. It is worth remembering that the spheroid assumption should be applied with proper particle size distribution and size dependent refractive index.

Table 2. The investigated cases in this study and their corresponding root mean square error of transmittance with respect to experimental result.

Case name	Root mean square error
Real sample	-
Spheroid assumption	2.9%
Sphere assumption	11.3%
Monodisperse assumption	9.4%
Bulk ref. index assumption	6.8%

5.4.Effect of plasmonic coupling

To demonstrate the significance of the coupling effect, we performed a case study, in which we first calculated the absorption cross-section of the digitized particle disk (**Figure 3(c)**) which has 824 spheroids. Then we calculated the absorption cross-sections of each 824 spheroids separately (without considering neighboring particles) and added the absorption cross-sections up. Error! Reference source not found. indicated that interparticle coupling effect resulted in a red shift as well as widening and damping in the absorption peak as expected [26].

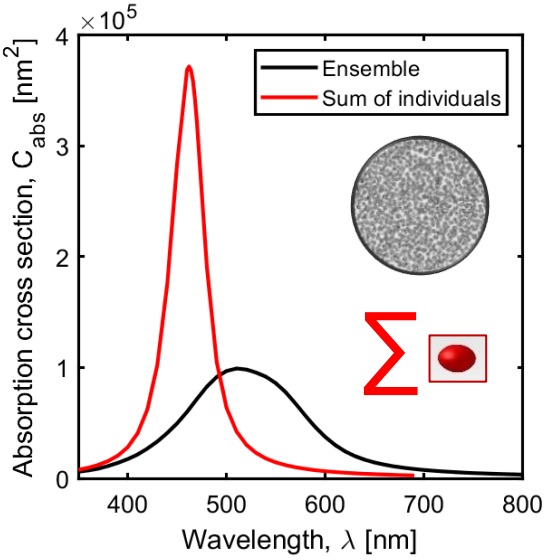

Figure 7. Absorption cross-section of the digitized particle disk (shown in **Figure 3(c)**) and cumulative individual absorption cross-sections of the spheroids inside the disk.

As described briefly in the problem statement, an additional case study is performed that gradually weakens the coupling effect to observe its effect on spectral characteristics like reflectance and color. 6 different "center to center inter-particle distance with the nearest neighbor", c_{min}, are chosen, as 10, 15, 20, 25, 30, 35 nm. Then, an algorithm that loops through each particle and shifts them upwards through the light source if they are close to another particle more than c_{min}. Their new location becomes [x_k, y_k, z_k+ c_{min}]. Algorithm starts with the digitized particle disk (**Figure 3(c)**) and spheres can shift to upper levels many times if they are still close to a particle more than c_{min}. This process is finished until it is ensured that no particle is close to the other more than c_{min}. **Figure 8** illustrates 6 different geometries are constructed with 6 different c_{min}. It is worth noting that all of the 6 different geometries have the same top view which is the same as **Figure 3(c)**.

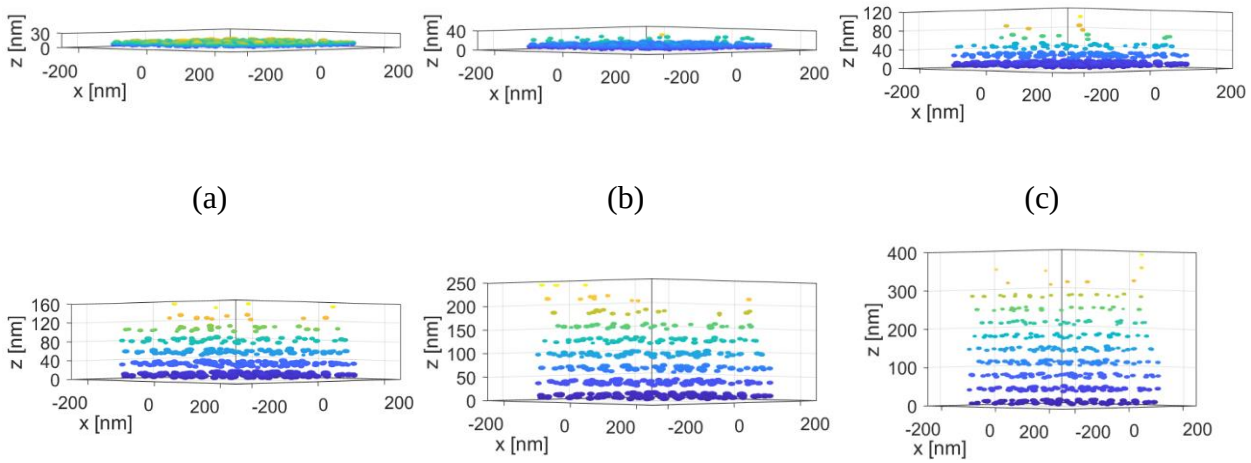

Figure 8. The resulting spatial distribution of NPs at (a) c_{min} = 10 nm, (b) c_{min} = 15 nm, (c) c_{min} = 20 nm, (d) c_{min} = 25 nm, (e) c_{min} = 30 nm, and (f) c_{min} = 35 nm.

Figure 6 illustrates the spectral transmittance for the multilayered case at c_{min} = 35 nm. The transmittance dip is much narrower and deeper compared to the single layered densely located particles. This behavior is promising for colored radiative cooling applications where high lightness, L, and low solar absorptance P_{solar} is favored. The case study for surface plasmons was also performed for the radiative cooling structure (**Figure 1(b)**) to observe the coupling effect on the structure's solar heat absorption and color. D65 illumination and a CIELUV standard representing the outside illumination accounting for the environment is considered while

calculating the corresponding color output. (ASTM) G-173 Reference Air Mass 1.5 Spectra is used for spectral solar intensity to calculate solar heat absorption. As the radiative cooling application requires, the back face of each design was coated with a 300 nm thick reflective bulk silver layer as shown in **Figure 1(b)**. Then, the corresponding simulated spectral reflectance of the six cases at different c_{min}, under unpolarized gaussian beam were calculated along with their resulting chromaticity coordinates (*u* and *v)*, lightness, (*L)* and radiative cooling [W m^{-2}]. **Figure 9(b)** illustrates the corresponding results. Calculation of chromaticity coordinates and lightness are given in the supplementary information. Presented results indicate that dilute multilayer designs were favorable. 44 W m^{-2} reduction of the solar heat absorption without decreasing the amount of silver NPs but only increasing their inter-particle distance is notable. It is worth mentioning that negative radiative cooling in **Figure 3(b)** corresponds to heating.

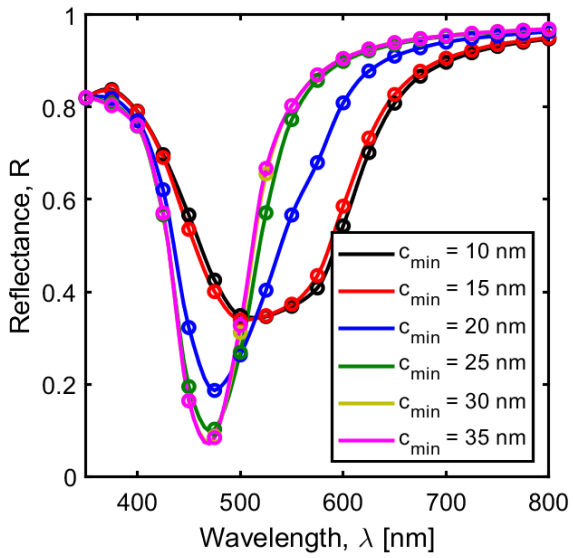

(a)

c_{min} = 10 nm Luv = [71.7, 34.7, -22.7] P_{solar} = 179 W m^{-2} P_{cool} = -41 W m^{-2}	c_{min} = 25 nm Luv = [87.5, 41.7, 61.9] P_{solar} = 141 W m^{-2} P_{cool} = -3 W m^{-2}
c_{min} = 15 nm Luv = [72.6, 38.8, -17.1] P_{solar} = 176 W m^{-2} P_{cool} = -38 W m^{-2}	c_{min} = 30 nm Luv = [89.0, 35.9, 67.8] P_{solar} = 136 W m^{-2} P_{cool} = 2 W m^{-2}
c_{min} = 20 nm Luv = [80.7, 51.4, 30.8] P_{solar} = 158 W m^{-2} P_{cool} = -20 W m^{-2}	c_{min} = 35 nm Luv = [89.1, 34.9, 68.23] P_{solar} = 135 W m^{-2} P_{cool} = 3 W m^{-2}

(b)

Figure 9. (a) Spectral reflectance of the radiative cooler (**Figure 1(b)**) as a function of wavelength at different c_{min} and (b) corresponding chromaticity coordinates, lightness, absorbed solar heat flux and total radiative cooling. Note that the background of the cells corresponds to the color outputs.

In our previous study [27], we showed that a post-deposition treatment using an ultra-low energy ion bombardment (<100eV) can be applied to obtain a dilute layer. This method can be applied after each silver deposition, then make a capping layer of dielectric layer then again silver

deposition followed by plasma treatment. This procedure can be repeated until each dilute layer is obtained.

6. Conclusion

This study demonstrates the significance of neighboring particles' coupling effects to the spectral absorption of metal islands. As an application, we investigated the metal islands as color introducing filters to radiative coolers. We found that considering multilayers of dilute silver NPs instead of a single dense layer was more efficient for introducing color to radiative cooling structures in terms of thermal efficacy and color implementation. Furthermore, we investigated the commonly considered assumptions while modeling electromagnetic radiation transfer through metal islands. The studied assumptions were using (i) oblate spheroid and (ii) spherical particles (iii) considering monodisperse size distribution, and finally (iv) using bulk refractive index for silver NPs. The effects of these assumptions were identified visually from spectral transmittance graphs and numerically by calculation of root mean square errors. We found that using these assumptions resulted in errors that can exceed 10% and therefore should be avoided for applications requiring a high accuracy. Finally, the contact angle of the NPs was set to 180° (non-wetting) in this study. In a future study, a realistic contact angle for spheroids can be investigated for a more accurate model.

Acknowledgement

We are grateful to Dr. David Lantiat for performing the HAADF-STEM characterizations. R.A.Y is also grateful for financial support from the Marie Skłodowska-Curie Actions Postdoctoral Individual Fellowship Program (project no: 892456)

References

[1] Raman AP, Anoma MA, Zhu L, Rephaeli E, Fan S. Passive radiative cooling below ambient air temperature under direct sunlight. Nature 2014;515:540–4. https://doi.org/10.1038/nature13883.

[2] Yalcin RA, Blandre E, Joulain K, Drévillon J. Colored Radiative Cooling Coatings with Nanoparticles. ACS Photonics 2020;7:1312–22. https://doi.org/10.1021/acsphotonics.0c00513.

[3] Yalçın RA, Blandre E, Joulain K, Drévillon J. Colored radiative cooling coatings with fluorescence. J Photonics Energy 2021;11. https://doi.org/10.1117/1.JPE.11.032104.

[4] Fabijanić I, Janicki V, Ferré-Borrull J, Bubaš M, Blažek Bregović V, Marsal LF, et al. Plasmonic Nanoparticles and Island Films for Solar Energy Harvesting: A Comparative Study of Cu, Al, Ag and Au Performance. Coatings 2019;9:382. https://doi.org/10.3390/coatings9060382.

[5] Freund H-J. Clusters and islands on oxides: from catalysis via electronics and magnetism to optics. Surf Sci 2002;500:271–99. https://doi.org/10.1016/S0039-6028(01)01543-6.

[6] Hoa XD, Kirk AG, Tabrizian M. Towards integrated and sensitive surface plasmon resonance biosensors: A review of recent progress. Biosens Bioelectron 2007;23:151–60. https://doi.org/10.1016/j.bios.2007.07.001.

[7] Takagi D, Homma Y, Hibino H, Suzuki S, Kobayashi Y. Single-Walled Carbon Nanotube Growth from Highly Activated Metal Nanoparticles. Nano Lett 2006;6:2642–5. https://doi.org/10.1021/nl061797g.

[8] Mie G. Beiträge zur Optik trüber Medien, speziell kolloidaler Metallösungen. Ann Phys 1908;330:377–445. https://doi.org/10.1002/andp.19083300302.

[9] Bohren CF, Huffman DR, editors. Absorption and Scattering of Light by Small Particles. Weinheim, Germany, Germany: Wiley-VCH Verlag GmbH; 1998. https://doi.org/10.1002/9783527618156.

[10] Mishchenko MI, Goldstein DH, Chowdhary J, Lompado A. Radiative transfer theory verified by controlled laboratory experiments. Opt Lett 2013;38:3522. https://doi.org/10.1364/OL.38.003522.

[11] Yee KS, Chen JS. The finite-difference time-domain (FDTD) and the finite-volume time-domain (FVTD) methods in solving Maxwell's equations. IEEE Trans Antennas Propag 1997;45:354–63. https://doi.org/10.1109/8.558651.

[12] Draine BT, Flatau PJ. Discrete-Dipole Approximation For Scattering Calculations. Journal of the Optical Society of America A 1994;11:1491. https://doi.org/10.1364/JOSAA.11.001491.

[13] Monk P. Finite Element Methods for Maxwell's Equations. Oxford University Press; 2003. https://doi.org/10.1093/acprof:oso/9780198508885.001.0001.

[14] Mackowski DW, Mishchenko MI. A multiple sphere T-matrix Fortran code for use on parallel computer clusters. J Quant Spectrosc Radiat Transf 2011;112:2182–92. https://doi.org/10.1016/j.jqsrt.2011.02.019.

[15] Baran AJ, Yang P, Havemann S. Calculation of the single-scattering properties of randomly oriented hexagonal ice columns: a comparison of the T-matrix and the finite-difference time-domain methods. Appl Opt 2001;40:4376. https://doi.org/10.1364/AO.40.004376.

[16] Egel A, Czajkowski KM, Theobald D, Ladutenko K, Kuznetsov AS, Pattelli L. SMUTHI: A python package for the simulation of light scattering by multiple particles near or between planar interfaces. J Quant Spectrosc Radiat Transf 2021;273:107846. https://doi.org/10.1016/j.jqsrt.2021.107846.

[17] Egel A, Pattelli L, Mazzamuto G, Wiersma DS, Lemmer U. CELES: CUDA-accelerated simulation of electromagnetic scattering by large ensembles of spheres. J Quant Spectrosc Radiat Transf 2017;199:103–10. https://doi.org/10.1016/j.jqsrt.2017.05.010.

[18] Mendoza Herrera LJ, Arboleda DM, Schinca DC, Scaffardi LB. Determination of plasma frequency, damping constant, and size distribution from the complex dielectric function of noble metal nanoparticles. J Appl Phys 2014;116:233105. https://doi.org/10.1063/1.4904349.

[19] Yuen H, Princen J, Illingworth J, Kittler J. Comparative study of Hough Transform methods for circle finding. Image Vis Comput 1990;8:71–7. https://doi.org/10.1016/0262-8856(90)90059-E.

[20] Babonneau D, Lantiat D, Camelio S, Toudert J, Simonot L, Pailloux F, et al. Gold and silver nanoparticles embedded in dielectric-capping layers studied by HAADF-STEM.

The European Physical Journal Applied Physics 2008;44:3–9. https://doi.org/10.1051/epjap:2008051.

[21] Theobald D, Beutel D, Borgmann L, Mescher H, Gomard G, Rockstuhl C, et al. Simulation of light scattering in large, disordered nanostructures using a periodic T-matrix method. J Quant Spectrosc Radiat Transf 2021;272:107802. https://doi.org/10.1016/j.jqsrt.2021.107802.

[22] Siegel R, Howell JR, Mengüç MP. Thermal radiation heat transfer. vol. 33. 2011. https://doi.org/10.1088/0022-3727/30/20/018.

[23] Wu Y, Zhang C, Estakhri NM, Zhao Y, Kim J, Zhang M, et al. Intrinsic Optical Properties and Enhanced Plasmonic Response of Epitaxial Silver. Advanced Materials 2014;26:6106–10. https://doi.org/10.1002/adma.201401474.

[24] Kitamura R, Pilon L, Jonasz M. Optical constants of silica glass from extreme ultraviolet to far infrared at near room temperature. Appl Opt 2007;46:8118. https://doi.org/10.1364/AO.46.008118.

[25] Kreibig U, Vollmer M. Optical Properties of Metal Clusters. vol. 25. Berlin, Heidelberg: Springer Berlin Heidelberg; 1995. https://doi.org/10.1007/978-3-662-09109-8.

[26] Jain PK, Huang W, El-Sayed MA. On the Universal Scaling Behavior of the Distance Decay of Plasmon Coupling in Metal Nanoparticle Pairs: A Plasmon Ruler Equation. Nano Lett 2007;7:2080–8. https://doi.org/10.1021/nl071008a.

[27] Simonot L, Chabanais F, Rousselet S, Pailloux F, Camelio S, Babonneau D. Evolution of plasmonic nanostructures under ultra-low-energy ion bombardment. Appl Surf Sci 2021;544:148672. https://doi.org/10.1016/j.apsusc.2020.148672.

Supplementary Information

S.1. Calculating the color

Estimation of the color is performed according to the position of eye. For radiative coolers (**Figure 1(b)**) normal reflected light, *R(0,λ)*. For the source, D65 CIE standard illuminant representing a phase of daylight with a correlated color temperature of approximately 6504 K. Spectrum to color conversion is then performed by using the CIELUV color space.

First, using the spectral reflected (or transmitted) intensity *R(0,λ) (or T(0,λ))* and the color matching functions ($\bar{x}(\lambda), \bar{y}(\lambda), \bar{z}(\lambda)$) that characterize the CIE 1931 Standard Colorimetric Observer, the tristimulus values *X, Y, Z* of the CIE 1931 color space, can be calculated as

$$X = 100 \frac{\int_{380\ nm}^{780\ nm} I_{D65}(\lambda)\, R(0,\lambda)\overline{x}(\lambda) d\lambda}{\int_{380\ nm}^{780\ nm} I_{D65}(\lambda)\, \overline{y}(\lambda) d\lambda} \tag{S1}$$

$$Y = 100 \frac{\int_{380\ nm}^{780\ nm} I_{D65}(\lambda)\, R(0,\lambda)\overline{y}(\lambda) d\lambda}{\int_{380\ nm}^{780\ nm} I_{D65}(\lambda)\, \overline{y}(\lambda) d\lambda} \tag{S2}$$

$$Z = 100 \frac{\int_{380\ nm}^{780\ nm} I_{D65}(\lambda)\, R(0,\lambda)\overline{z}(\lambda) d\lambda}{\int_{380\ nm}^{780\ nm} I_{D65}(\lambda)\, \overline{y}(\lambda) d\lambda} \tag{S3}$$

Chromaticity co-ordinates x, y ,z parameters can be used to identify the color in chromacity diagram. They are defined as;

$$x = \frac{X}{X + Y + Z} \tag{S9}$$

$$y = \frac{Y}{X + Y + Z} \tag{S10}$$

$$z = \frac{Z}{X + Y + Z} \tag{S11}$$

Then the CIELUV color space parameters, CIE1976 lightness L*, redness - greenness u*, and yellowness - blueness v*, are given as

$$u' = \frac{4X}{X + 15Y + 3Z}$$

$$v' = \frac{9Y}{X + 15Y + 3Z}$$

$$L^* = \begin{cases} \left(\frac{29}{3}\right)^3 Y/Y_n - 16 \quad if \quad Y/Y_n \leq \left(\frac{6}{29}\right)^3 \\ 116\,(Y/Y_n)^3 - 16 \quad if \quad Y/Y_n > \left(\frac{6}{29}\right)^3 \end{cases} \tag{S13}$$

$$u^* = 13L^*[u' - u'_n] \tag{S14}$$

$$v^* = 13L^*[v' - v'_n] \tag{S15}$$

S.2. Selecting spherical harmonics order, l_{max}

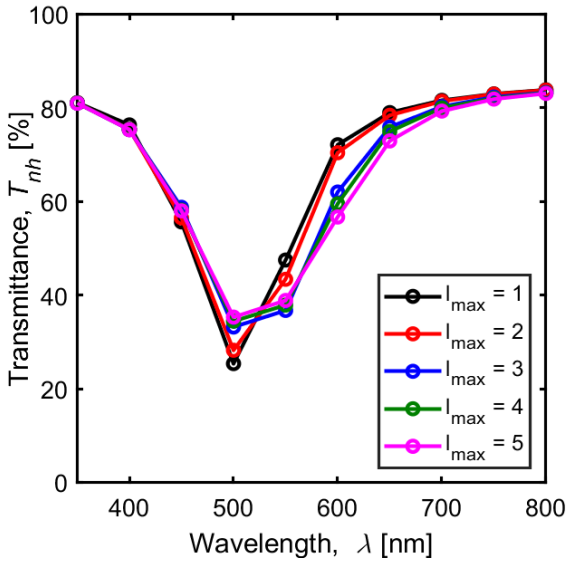

Figure S1. Spectral transmittance as a function of wavelength at different l_{max}.

S.3. Applicability conditions for the T-matrix method

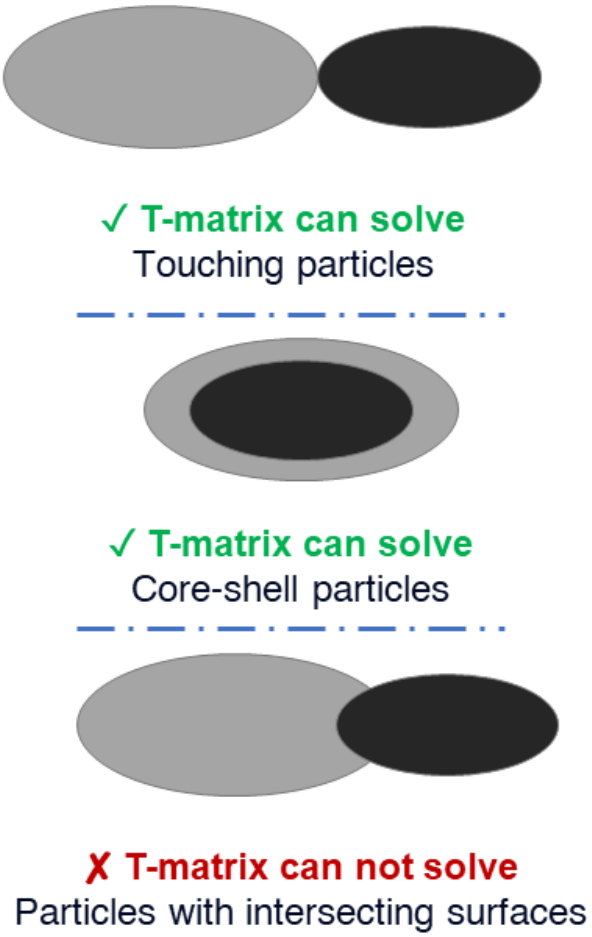

Figure S2. Validity of T-matrix method.

S.4. Fabricated colored radiative cooler

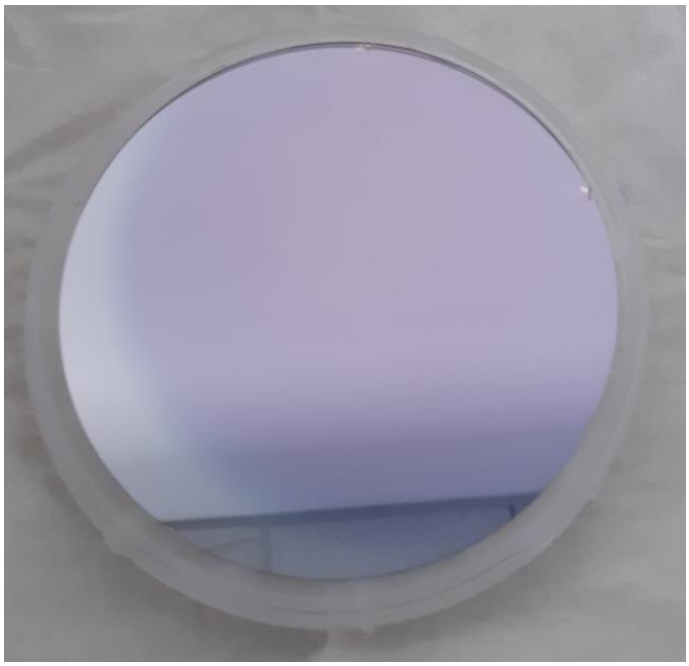

Figure S3. Fabricated colored radiative cooler by deposing silver NPs over silica and coating it with Al_2O_3. Finally, coating the other side (silica) with silver layer. Purplish color is obtained as we estimated using the T-matrix method.

S.5. Particle size dependent optical properties and characteristics

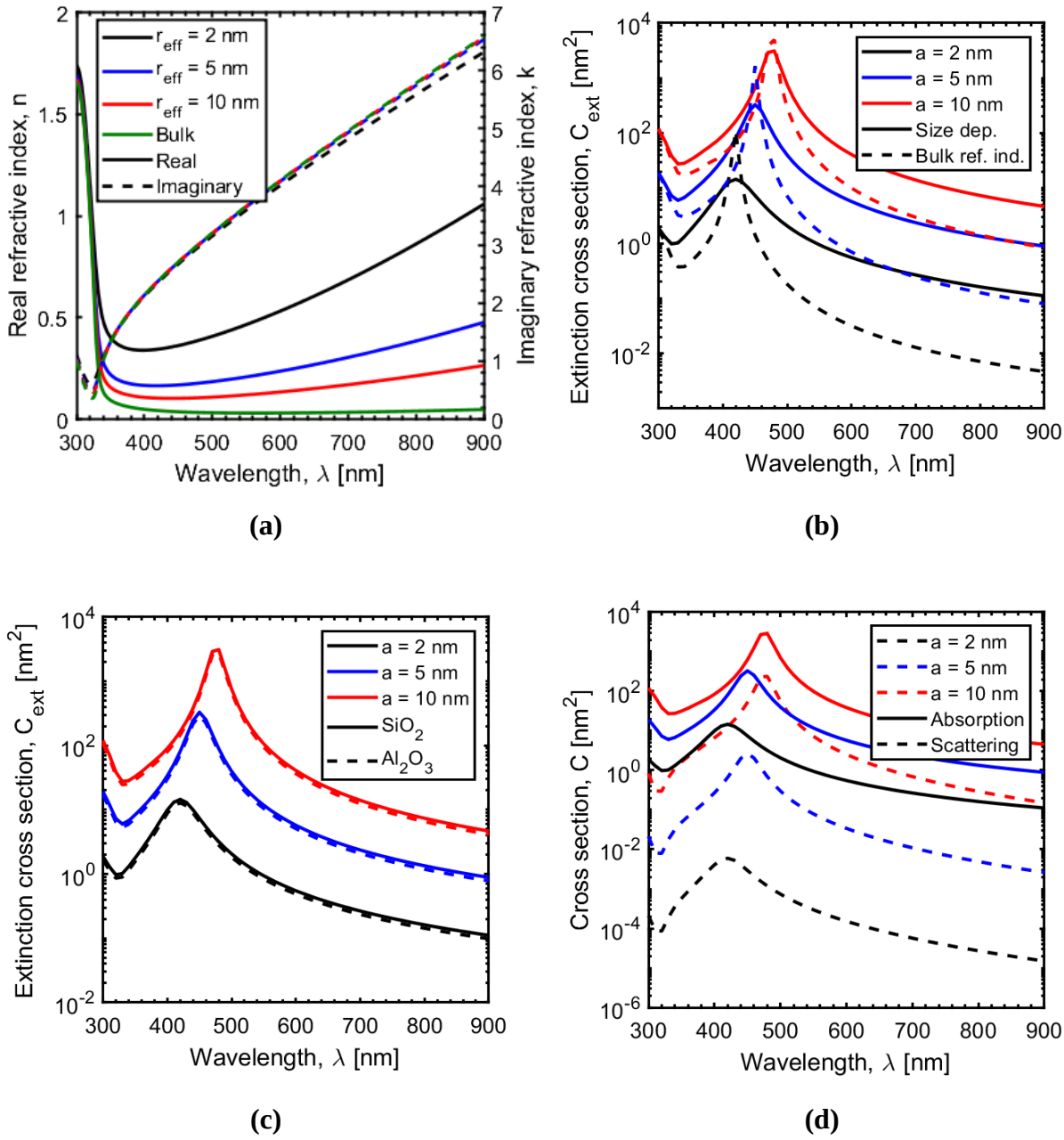

Figure S4. (a) Spectral real (solid) and imaginary (dashed) refractive indices of bulk silver and silver nano particles at 2 nm, 5 nm and 10 nm radii. For those sizes; (b) calculated spectral extinction cross sections of a single particle on silica, capped by alumina under normal incidence with plane wave when size dependent (solid line) and bulk (dashed line) refractive indices are used, (c) calculated spectral extinction cross sections of alumina capped single particle sitting on

silica (solid line) and alumina (dashed line), and (d) calculated spectral absorption (solid line) and scattering (dashed line) cross sections of alumina capped single particle sitting on silica.